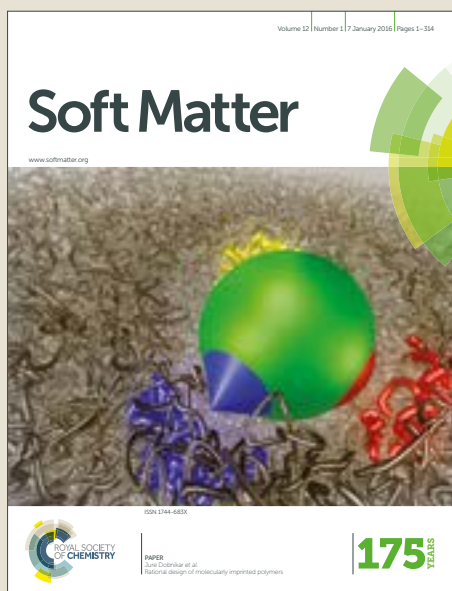


Soft Matter

Accepted Manuscript



This article can be cited before page numbers have been issued, to do this please use: H. Perrin, R. Lhermerout, K. Davitt, E. Rolley and B. Andreotti, *Soft Matter*, 2018, DOI: 10.1039/C7SM02211E.



This is an Accepted Manuscript, which has been through the Royal Society of Chemistry peer review process and has been accepted for publication.

Accepted Manuscripts are published online shortly after acceptance, before technical editing, formatting and proof reading. Using this free service, authors can make their results available to the community, in citable form, before we publish the edited article. We will replace this Accepted Manuscript with the edited and formatted Advance Article as soon as it is available.

You can find more information about Accepted Manuscripts in the [author guidelines](#).

Please note that technical editing may introduce minor changes to the text and/or graphics, which may alter content. The journal's standard [Terms & Conditions](#) and the ethical guidelines, outlined in our [author and reviewer resource centre](#), still apply. In no event shall the Royal Society of Chemistry be held responsible for any errors or omissions in this Accepted Manuscript or any consequences arising from the use of any information it contains.

Cite this: DOI: 10.1039/xxxxxxxxxx

Thermally activated motion of a contact line over defects

Hugo Perrin^a, Romain Lhermerout^a, Kristina Davitt^a, Etienne Rolley^a and Bruno Andreotti^a

Received Date
 Accepted Date

DOI: 10.1039/xxxxxxxxxx

www.rsc.org/journalname

At the nanometer scale, the motion of a contact line separating a dry from a wet region is limited by the presence of surface heterogeneities that pin it. Here we revisit the seminal model proposed by Joanny and de Gennes to include the influence of thermal noise and viscosity using a Langevin model with two degrees of freedom: the average position of the contact line and its distortion. We identify the conditions under which the dynamics in a velocity-driven experiment can in fact be described by a constant forcing at small scale. We then relate the asymptotic properties of the relation between force and contact line velocity to the properties of the defects. In particular, we show that Kramers' approximation misses the strong asymmetry between advancing and receding directions. Finally, we show how to use the model to fit experimental data and extract the salient features of the surface energy landscape.

1 Introduction

A liquid drop moving over a solid surface is an everyday occurrence yet a complete theoretical description of the observed motion is lacking. We know the basic ingredients that must go into understanding the dynamics of the three-phase contact line at the edge of the drop^{1–3}: there is both viscous dissipation in the bulk of the liquid meniscus, occurring at all scales between the molecular scale and the capillary length, and a dissipation that occurs at the nanometer scale, in the vicinity of the contact line. The former is fully described by hydrodynamic theory. The latter is due to thermally activated jumps over molecular-scale discreteness⁴ or inevitable nano-scale inhomogeneities that pin the line on the surface⁵, processes that have been studied by various computational methods at the molecular scale^{6,7} but which are most often reduced to an Arrhenius-type expression^{4,8,9}. In addition, depending on the specific nature of the liquid and solid combination, there may be other effects to consider, such as reactive wetting^{10,11} or visco-elastic dissipation¹², each of which has been studied independently. Wetting experiments that mea-

sure the variation of a contact angle θ with the velocity U of the contact line, such as shown in Fig. 1, can therefore contain a rich phenomenology. In practice, however, even the simplest case of a liquid moving over an apparently homogeneous solid surface – where one expects only hydrodynamics and thermal-activation – interpreting the full experimentally-observed dynamics remains challenging. For example, contact angle hysteresis is usually thought to be related to the critical mechanical force needed to unpin the contact line from defects. However, it is not clear how to locate the critical or *depinning* point, which plays a central role in theories based on the depinning of an elastic line on a frozen stochastic landscape^{13,14}, in a measured dynamics curve. This arises from the disconnect between the theoretical concept of depinning in the quasi-static, athermal limit, and the method most commonly used in practice to measure the difference between advancing and receding angles at a low, but arbitrarily chosen, velocity and at room temperature. To resolve such issues, a complete description of thermally activated processes beyond the limits of the Arrhenius expression is needed.

Previously, we reported a framework to unify hydrodynamics and thermal activation¹⁵. In this picture, the boundary condition at the solid surface, which is required by hydrodynamics, is provided by a microscopic contact angle θ_μ (defined at molecular scales) that takes into account the average effect of thermal activation over defects on the solid. The selection of θ_μ is modeled separately using a Langevin equation on the contact line position. The vocation of the present article is to explicitly develop and study this stochastic equation. In so doing, we will show how the

^a Laboratoire de Physique Statistique (LPS), UMR 8550 CNRS, ENS, Univ. Paris Diderot, Sorbonne Université, 24 rue Lhomond, 75005, Paris, France.

† Electronic Supplementary Information (ESI) available: [details of any supplementary information available should be included here]. See DOI: 10.1039/C7SM00000X/

‡ Additional footnotes to the title and authors can be included e.g. 'Present address:' or 'These authors contributed equally to this work' as above using the symbols: ‡, §, and ¶. Please place the appropriate symbol next to the author's name and include a \footnotetext entry in the the correct place in the list.

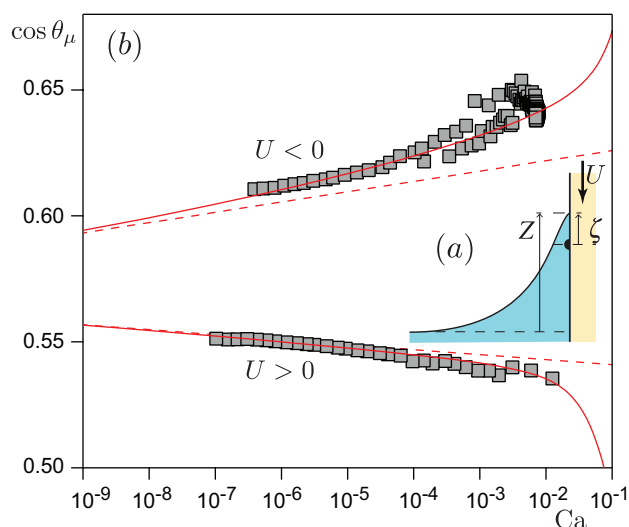


Fig. 1 (a) Schematic of a dip-coating experiment. By convention, the velocity U is positive when the solid plate is plunged into the bath and the contact line is advancing. Z is the mean altitude of the contact line above the bath. ζ is the mean position of the contact line with respect to the plate, whose frame of reference has an origin centered on a defect. (b) Typical experimental relation (markers) between the microscopic contact angle θ_μ and the capillary number, taken from¹⁵. The solid line represents the best fit to the full four-parameter model that we develop in this article. The dashed line corresponds to the asymptotic regime at low temperature for the same physical parameters.

model answers some unresolved experimental questions.

Contact line dynamics can be measured by a variety of methods in a variety of geometries, from looking at the relaxation of a drop in profile as it impinges on a solid surface^{16,17} to the pulling of a solid fiber^{18,19} or plate^{8,20} into or out of a liquid bath. In all cases, the aim is to determine the relationship between the contact line velocity U – or the capillary number $Ca = \eta U / \gamma$ – and the dynamic contact angle, or more generally, the unbalanced Young force. Models on a single defect have predicted a dynamics that depends on whether the velocity of the contact line or the force exerted upon it are imposed²¹. For any given experimental realization, one can ask what is the control parameter. The answer to this simple question is in fact not so straightforward. As an example, we examine the classic dip-coating setup where the speed at which the solid plate is plunged into or pulled out of the bath is controlled by a motorized stage. In this case, the stage determines the time-averaged contact line velocity U but not necessarily either its instantaneous velocity or even its instantaneous spatial average. Indeed, such experiments yield dynamics that are well fitted by a Langevin model under constant *force*. Here we will show that the dynamics for constant-velocity driving in fact reduce to constant-force when the stiffness of the meniscus²² is small, which is the case for dip-coating a plate. This explains the observation of a logarithmic activation law relating the driving force to the capillary number (Fig. 1) even though one is not expected for constant-velocity driving. We perform a parametric study of this case to find the dependence of the slopes in the logarithmic regime, and of the asymmetry between the advancing and receding branches, on the defect width and amplitude and on the

thermal noise.

The development of this model traces its origin to the desire to extend the model of Joanny and de Gennes²³ for contact angle hysteresis in order to take account of thermal activation⁸. They considered the balance between the pinning force of the defect and the elastic restoring force of a distorted contact line. Considering an individual defect, they classified it as either weak or strong depending on the multistability of the force balance, or in other words, whether the deformation of the contact line was reversible or not when advancing versus receding. Multistability can also occur due to collective effects, even for defects that would individually be considered as weak, due to the interaction between defects mediated by the contact line²⁴. This multistability in the detailed shape of the contact line (its deformation) results in a different contact angle, or force, depending on whether the contact line is advancing or receding when it is at the same average location; this is a true hysteresis of the deformation of the contact line. For monostable weak defects there is no such hysteresis in the deformation. However, we will show that one still obtains a separation between the two branches of the dynamics such as that shown in Fig. 1. This arises from the energy landscape along the reaction coordinate, which is monovalued but still not flat. It explains the existence of a minimum force required to depin the contact line from the defect (at zero temperature), which, in addition, can be modified by thermally activated processes.

We begin by writing a coupled set of Langevin equations for the average position and the deformation of the contact line. Later, we show that for weak defects it can be reduced to a single variable. Alone, the extension of the model to two variables is an important step on the way to developing a complete model to handle strong defects, which present additional computational difficulties due to their multistability.

2 Development of the Langevin model

2.1 Introduction to the Langevin model

Our goal is to develop a simple model of thermally activated motion of a contact line over defects. We consider a liquid moving over a flat solid surface covered with chemical heterogeneities. We model an actual disordered substrate using a minimalist energy landscape of Gaussian defects of size d that are periodically spaced by a distance λ (Fig. 2). The intention is to find a simple way to model the energy landscape resulting from the dynamics over random energy landscapes. The periodic, Gaussian parameters correspond to an effective or mean-field defect rather than the real physical features on a surface. Using the reaction path approach, we project the multi-dimensional problem onto a low dimensionality problem. All but two degrees of freedom are assumed to relax quickly to equilibrium leaving only the average absolute position of the contact line ζ and the amplitude of the deformation of the contact line ψ . In this first section, we will show that the resulting system of Langevin equations can be written in the form:

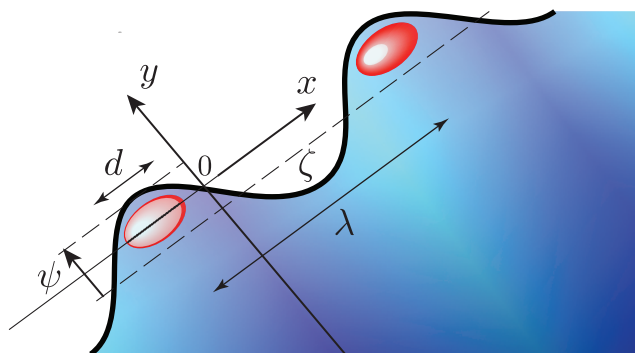


Fig. 2 Illustration of a contact line that is deformed as it passes over a periodic array of chemical defects of dimension d and separated by a wavelength λ . The defects are more wettable than the background: $\mathcal{C} > 0$ in the notation defined by eqn (16).

$$\begin{aligned} d_\psi \eta \dot{\psi} &= -\frac{1}{\lambda} \frac{\partial \mathcal{U}}{\partial \psi} + \sqrt{\frac{2d_\psi \eta k_B T}{\lambda}} \mathcal{W}_\psi(t) \\ d_\zeta \eta \dot{\zeta} &= \gamma F - \frac{1}{\lambda} \frac{\partial \mathcal{U}}{\partial \zeta} + \sqrt{\frac{2d_\zeta \eta k_B T}{\lambda}} \mathcal{W}_\zeta(t), \end{aligned} \quad (1)$$

where η is the viscosity, γ the surface tension, $\dot{\zeta}$ denotes the contact line velocity and $\dot{\psi}$ the time derivative of the disturbance amplitude. The last term in each equation corresponds to the thermal fluctuations, which are approximated by a Gaussian noise delta-correlated in time: $\langle \mathcal{W}_\psi(t) \mathcal{W}_\psi(t') \rangle = \delta(t - t')$ and $\langle \mathcal{W}_\zeta(t) \mathcal{W}_\zeta(t') \rangle = \delta(t - t')$. The multiplicative factors in front of the noise result from the fluctuation-dissipation theorem, using the equipartition of energy in the homogeneous situation. k_B the Boltzmann constant and T the temperature. The two noise terms are assumed to be independent, such that $\langle \mathcal{W}_\psi(t) \mathcal{W}_\zeta(t') \rangle = 0$. γF is the driving force per unit length, exerted by the outer part of the liquid. Its precise nature will be discussed in the next section. \mathcal{U} is the reduced free energy associated with the two degrees of freedom ψ and ζ :

$$\mathcal{U}(\psi, \zeta) = \gamma \left[\mathcal{C} \lambda d \sqrt{\frac{\pi}{2}} \operatorname{erf} \left[\frac{\zeta + \psi}{d\sqrt{2}} \right] + \pi \kappa \psi^2 \right]. \quad (2)$$

The error function term arises from the Gaussian distribution of solid surface tension used to describe chemical defects. The dimensionless number \mathcal{C} characterizes the defect strength. The effective quadratic energy $\pi \kappa \psi^2$ is associated with a linear restoring force that resists distortions of the contact line and originates from the surface energy of the liquid-vapor interface. The dimensionless constant κ is the spring constant of the deformation. The dimensionless damping factors d_ψ and d_ζ reflect the dissipation associated with the two types of contact line motion: the deformation and the global motion.

In this section we explicitly develop these equations, emphasizing physical arguments and simplifying assumptions made where needed in order to make the problem tractable. First we consider the free energy in order to express the conservative forces, then we discuss how to express the force of the outer meniscus – which is the driving term – then finally we address how to ap-

propriately express the dissipative constants. The remainder of the article investigates the dynamics described by eqn (1). First, in section (3) we show that the description can be reduced to a single degree of freedom and how to determine whether a given experimental realization is force-driven or velocity-driven. Then, section (4) is dedicated to a parametric study of the force-driven, single reaction-coordinate equation where the goal is to develop an expression for the purely logarithmic regime of the dynamics at asymptotically low temperature. Finally, section (5) addresses how to appropriately find the relevant fit parameters from experimental data.

2.2 Free energy functional

Here we consider how to express the free energy associated with substrate heterogeneities. Later this will allow us to develop expressions for the conservative forces that appear in eqn (1). As shown in Fig. 2, we decompose the profile of the contact line position into $\zeta + \psi \varepsilon(x)$, where $\varepsilon(x)$ is a dimensionless, zero-average function that we call the rescaled shape. The deformation ψ is measured by averaging the contact line deformation over a scale d . For this purpose, we introduce a weight function $w(x)$ normalized to 1 and that satisfies the condition $\int_{-\infty}^{+\infty} dx w(x) \varepsilon(x) = 1$. It will be later shown that this weight function reflects the spatial distribution of the dissipative forces and for Gaussian defects it takes the form:

$$w(x) = \frac{\exp \left[-\frac{x^2}{2d^2} \right]}{d\sqrt{2\pi}}. \quad (3)$$

We then write the total free energy of the system, which results from the free energy of the three interfaces. We introduce the free energy \mathcal{U}_S associated with the solid-vapor and solid-liquid interfaces. Taking the solid-vapor interface as the reference state for the solid, the free energy \mathcal{U}_S appears to be the excess free energy associated with the presence of liquid in the region $y < \zeta + \psi \varepsilon(x)$. Introducing the surface tensions γ_{SV} and γ_{SL} of the solid-vapor and solid-liquid interfaces, we obtain:

$$\mathcal{U}_S = \int_{-\infty}^{+\infty} dx \int_{-\infty}^{\zeta + \psi \varepsilon(x)} dy (\gamma_{SL}(x, y) - \gamma_{SV}(x, y)) \quad (4)$$

$$= - \int_{-\infty}^{+\infty} dx \int_{-\infty}^{\zeta + \psi \varepsilon(x)} dy \gamma \cos \theta_Y(x, y) \quad (5)$$

where $\theta_Y(x, y)$ is the Young-angle landscape, defined locally by $\gamma \cos \theta_Y = \gamma_{SV} - \gamma_{SL}$. In the following, we retain the angle notation rather than using the solid surface tensions.

We decompose the liquid-vapor energy into a contribution due to the large-scale shape of the interface and an excess \mathcal{U}_μ due to the small-scale fluctuations of the contact line. The macroscopic contribution to the energy does not depend on the disturbance amplitude ψ but only on the average position ζ of the contact line. If the large-scale shape of the liquid interface is simply flat, forming a liquid wedge of angle θ_μ , then it would take the form $\gamma \lambda \zeta \cos \theta_\mu$, leading to a dimensionless driving force per unit length:

$$F = -\cos \theta_\mu. \quad (6)$$

Here we denote the angle as θ_μ since we are interested in the

effective contact angle that the liquid makes with the solid measured at the microscopic scale, due to the average effect of thermally activated processes across heterogeneities. This is in contrast with experiment, where one has access to an angle that is defined at macroscopic scales and which therefore potentially contains dynamics associated with viscous dissipation in the bulk meniscus. We have previously shown how θ_μ can be deduced from experimental measurements¹⁵. Although the large-scale shape of the liquid interface is in fact not flat, we will see in the next section that even in a velocity-driven experiment such as a dip coating experiment, one can use the constant-force model described by eqn (6).

To compute the small-scale deformation of the contact line, we consider that the degrees of freedom associated with this shape relax to equilibrium over timescales that are small compared to the activation time. We focus on a single defect and introduce Fourier transforms along x , the direction transverse to global motion of the contact line:

$$\hat{\varepsilon}(q) = \int_{-\infty}^{+\infty} dx e^{-iqx} \varepsilon(x), \quad \varepsilon(x) = \int_{-\infty}^{+\infty} \frac{dq}{2\pi} e^{iqx} \hat{\varepsilon}(q). \quad (7)$$

We keep in mind that the case of periodic defects corresponds to discrete wave vectors $q = 2\pi p/\lambda$ parametrized by the integer p . We solve the Laplace equation for the interface under small distortions of the contact line²³, but for arbitrary large slopes. For a given mode q , the interface elevation profile takes the form: $-\tan \theta_\mu \psi \hat{\varepsilon}(q) e^{-|q|\lambda/\cos \theta_\mu}$, where θ_μ is the angle of the liquid-vapor interface averaged over the spatial fluctuations. The energy cost associated with the deformation of the liquid interface therefore reads:

$$\mathcal{U}_\mu = \frac{\gamma \psi^2 \sin^2 \theta_\mu}{2} \int_{-\infty}^{+\infty} \frac{dq}{2\pi} |q| |\hat{\varepsilon}(q)|^2. \quad (8)$$

Finally, we introduce two Lagrange multipliers (f and g) to achieve the decomposition of the contact line shape into the sum of ζ and of $\psi \varepsilon(x)$. The free energy function associated with the substrate heterogeneities reads:

$$\begin{aligned} \mathcal{U} &= \mathcal{U}_S + \mathcal{U}_\mu + f \gamma \psi \int_{-\infty}^{+\infty} \varepsilon(x) dx \\ &+ g \gamma \psi \left(\int_{-\infty}^{+\infty} w(x) \varepsilon(x) dx - 1 \right). \end{aligned} \quad (9)$$

2.3 Rescaled contact line profile

Now we seek to determine the rescaled profile of the contact line, $\varepsilon(x)$, considering that it relaxes faster than ζ and ψ . We therefore compute the variation of free energy with respect to $\varepsilon(x)$, which can be simply interpreted as a force balance.

$$\frac{\delta \mathcal{U}}{\delta \varepsilon(x)} = \frac{\delta \mathcal{U}_S}{\delta \varepsilon(x)} + \frac{\delta \mathcal{U}_\mu}{\delta \varepsilon(x)} + f \gamma \psi + g \gamma \psi w(x) = 0, \quad (10)$$

with

$$\frac{\delta \mathcal{U}_S}{\delta \varepsilon(x)} = -\gamma \psi \cos \theta_Y(x, \psi \varepsilon(x) + \zeta). \quad (11)$$

Following Joanny and de Gennes²³, we argue that since the pinning force is highly localized on the defect, the variation of θ_Y is dominated by what happens at the defect and the detailed variation due to the shape of the contact line around it can be neglected. In other words, the variation in θ_Y essentially takes place along x and we take the amplitude of the deformation to be the maximum ψ at all x :

$$\cos \theta_Y(x, \psi \varepsilon(x) + \zeta) \simeq \cos \theta_Y(x, \psi + \zeta). \quad (12)$$

The second functional derivative in eqn (10) is determined in Fourier space:

$$\frac{\delta^2 \mathcal{U}_\mu}{\delta \hat{\varepsilon}(q)} = \frac{\gamma \psi^2 \sin^2 \theta_\mu |q| \hat{\varepsilon}(-q)}{2\pi}, \quad (13)$$

where we have used the fact that $\varepsilon(x)$ is real. The equations then reduce to the force balance:

$$f + g w(x) = \cos \theta_Y(x, \psi + \zeta) - \psi \sin^2 \theta_\mu \int_{-\infty}^{+\infty} \frac{dq}{2\pi} \hat{\varepsilon}(q) |q| e^{iqx}, \quad (14)$$

where for internal consistency

$$\int_{-\infty}^{+\infty} dx' \frac{\varepsilon(x')}{(x-x')^2} \propto \cos \theta_Y(x, \psi + \zeta) - \langle \cos \theta_Y(x, \psi + \zeta) \rangle \quad (15)$$

with $\langle \cdot \rangle$ signifying an average over x

2.4 Gaussian defects

To progress further, one must specify the surface energy landscape explicitly. Here we consider Gaussian defects defined by:

$$\cos \theta_Y(x, y) = \cos \theta_S + \mathcal{C} \frac{\lambda}{d\sqrt{2\pi}} \exp \left[-\frac{x^2 + y^2}{2d^2} \right], \quad (16)$$

where $\cos \theta_S$ is a reference value corresponding to the Young angle that would be reached on the background surface far from a defect and \mathcal{C} is the scale-free magnitude of the defects. In what follows, we assume $\mathcal{C} > 0$, that is, defects that are more wettable than the background. Since we model effective defects, this is not a limiting assumption. What is a defect and what is the background is a matter of perspective: a less wettable defect can also be regarded as the background state, in which case the background becomes a more wettable defect. Then, $w(x)$ follows as:

$$w(x) = \frac{\exp \left[-\frac{x^2}{2d^2} \right]}{d\sqrt{2\pi}}. \quad (17)$$

For the 0 mode, the equilibrium condition eqn (14) thus gives

$$f + \frac{g}{\lambda} = \cos \theta_S + \mathcal{C} \exp \left[-\frac{(\psi + \zeta)^2}{2d^2} \right], \quad (18)$$

where we have used λ as the large-scale cut-off ensuring finite integrals, within the approximation of small defects $d \ll \lambda$. For the other Fourier modes, one obtains:

$$\hat{\varepsilon}(q) = A \frac{\exp \left[-(qd)^2/2 \right]}{|q|}, \quad (19)$$

where A is a normalization constant that is a function of λ/d . From the constraint $\int_{-\infty}^{+\infty} dx w(x) \varepsilon(x) = 1$, and again assuming that $d \ll \lambda$, we find:

$$A = \left[\int_{-\infty}^{+\infty} \frac{dq}{2\pi} \frac{\exp[-(qd)^2]}{|q|} \right]^{-1} \simeq \frac{\pi}{\ln(\lambda/2\pi d)}. \quad (20)$$

Finally, the shape of the contact line pinned on a localized defect depends logarithmically on space, according to:

$$\varepsilon(x) \sim \frac{\ln\left(\frac{\lambda}{2\pi(d+|x|)}\right)}{\ln\left(\frac{\lambda}{2\pi d}\right)}. \quad (21)$$

2.5 Conservative forces

Derivatives of the free energy with respect to ζ and ψ provide the conservative force terms that will appear in the dynamic equations governing each of these two degrees of freedom. Starting with ζ , we find:

$$\left. \frac{\partial \mathcal{U}}{\partial \zeta} \right|_{\psi} = -\gamma \lambda \langle \cos \theta_Y \rangle, \quad (22)$$

which is the force due to the large-scale liquid-vapor interface. For the Gaussian defects used here, we can further write the spatial average

$$\langle \cos \theta_Y \rangle = \cos \theta_S + \mathcal{C} \exp\left(-\frac{(\zeta + \psi)^2}{2d^2}\right). \quad (23)$$

For ψ :

$$\left. \frac{\partial \mathcal{U}}{\partial \psi} \right|_{\zeta} = -\gamma \lambda \langle \varepsilon \cos \theta_Y \rangle + \gamma \psi \sin^2 \theta_{\mu} \int_{-\infty}^{+\infty} \frac{dq}{2\pi} |q| |\hat{\varepsilon}(q)|^2. \quad (24)$$

Introducing the effective spring constant of the distortions of the contact line κ , given by

$$\begin{aligned} \kappa &\equiv \frac{\sin^2 \theta_{\mu}}{2\pi} \int_{-\infty}^{+\infty} \frac{dq}{2\pi} |q| |\hat{\varepsilon}(q)|^2 \\ &= \frac{\sin^2 \theta_{\mu}}{2\pi} A \sim \frac{\sin^2 \theta_{\mu}}{2 \ln(\lambda/2\pi d)}. \end{aligned} \quad (25)$$

We rewrite the derivative of the free energy \mathcal{U} with respect to ψ as:

$$\left. \frac{\partial \mathcal{U}}{\partial \psi} \right|_{\zeta} = -\gamma \lambda \mathcal{C} \exp\left[-\frac{(\psi + \zeta)^2}{2d^2}\right] + \gamma 2\pi \kappa \psi. \quad (26)$$

2.6 The driving term

In the free energy associated with substrate heterogeneities, \mathcal{U}_{μ} accounted for the liquid-vapor interface energy contribution coming from small scale fluctuations of the contact line. The goal of this section is to develop an expression for the force exerted by the rest of the outer liquid meniscus, which is the driving term.

First we linearize the elastic restoring force $F = -\cos \theta$ around the time-averaged position of the contact line with respect to the bath \bar{Z} . In a typical dip-coating experiment, a solid plate is plunged in the liquid bath at a constant imposed velocity U . Up

to a constant, equivalent to the choice of definition for $t = 0$, the altitude of the meniscus above the bath Z is related to the contact line position ζ (whose frame of reference is that of the plate) by the equation: $Z = -Ut + \zeta$. The instantaneous force of the meniscus interface then takes the form

$$F = -\cos \theta_{\mu} + k_{\zeta}(\bar{Z} - Z) = -\cos \theta_{\mu} + k_{\zeta}(\bar{Z} + Ut - \zeta), \quad (27)$$

and an appropriate expression for the spring constant of the elastic restoring force k_{ζ} must be found.

In the case of a contact line moving quasi-statically, the effective spring constant of the meniscus around equilibrium is found from eqn (6) and the contact line altitude above the bath $Z = \ell_{\gamma} \sqrt{2(1 - \sin \theta_{\mu})}$. One obtains

$$k_{\zeta} = \frac{\partial F}{\partial Z} = \frac{\tan \theta_{\mu} \sqrt{2(1 - \sin \theta_{\mu})}}{\ell_{\gamma}}, \quad (28)$$

where the capillary length is

$$\ell_{\gamma} = \sqrt{\frac{\gamma}{\rho g}}. \quad (29)$$

In this quasi-static case the fluctuations of the contact line deform the meniscus over its full extent (proportional to ℓ_{γ}). At higher frequencies, however, the disturbance induced by the intermittent motion is limited and far from the contact line the liquid-vapor interface may appear undisturbed. The characteristic penetration length ℓ_U depends on the mean angular frequency ω at which the contact line oscillates²⁵. Using a geometrical reasoning from Fig. 3, one can show that the spring constant k_{ζ} is inversely proportional to the length ℓ_U :

$$k_{\zeta} \sim \frac{\partial \theta}{\partial Z} \sim \frac{3}{\ell_U \tan \theta_{\mu}}, \quad (30)$$

where the complete derivation detailed in reference²⁵ gives the dependence of k_{ζ} on θ_{μ} . In order to find a scaling law for the penetration length, we dimensionally balance the viscous stress $\tau \sim \eta \omega (Z - \bar{Z}) / \ell_U$ and the Laplace pressure $P \sim \gamma (\cos \theta - \cos \theta_{\mu}) / \ell_U$. Again using the geometry in Fig. 3, the latter is seen to scale as $P \sim \gamma (\bar{Z} - Z) / \ell_U^2$, and thus we find

$$\ell_U \sim \frac{\gamma}{\eta \omega}. \quad (31)$$

In principle, oscillations of the contact line occur over a spectrum of frequencies. To render the problem tractable, we assume a single dominant frequency. Here we are concerned with the restoring force on the global motion and therefore we take a frequency that corresponds to the rate at which the contact line moving at a mean velocity U crosses energy barriers: $\omega \sim 2\pi U / \lambda$. This and eqn (31) into eqn (30) give

$$k_{\zeta} \sim \frac{6\pi\eta|U|}{\gamma\lambda \tan \theta_{\mu}}. \quad (32)$$

At higher velocity, the dynamically fluctuating meniscus is stiffer than the static one described by eqn (28) and therefore dominates the force. The cross-over between a dynamic and a

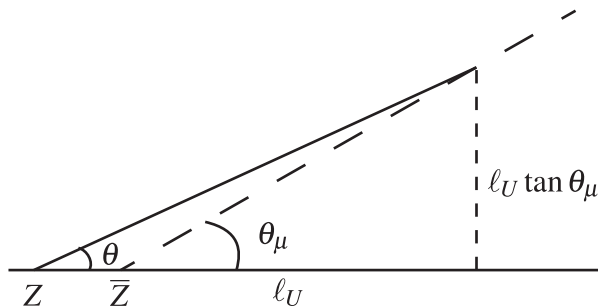


Fig. 3 Illustration of the meniscus in the frame of reference of the bath and viewed at a scale smaller than the capillary length. The dashed line is the time-averaged meniscus. The fluctuations of the contact line position Z around its time average \bar{Z} only disturb the meniscus over a penetration length $\sim \ell_U$. The instantaneous force $F = -\cos \theta$ can be linearized around \bar{Z} to give eqn (27).

static regime is obtained by equating the two expressions:

$$\text{Ca}_{\text{co}} \sim \frac{\tan^2 \theta_\mu \sqrt{2(1 - \sin \theta_\mu)}}{6\pi} \frac{\lambda}{\ell_\gamma}. \quad (33)$$

In the case of the experiment associated with the data shown in Fig. 1 we find $\sim 10^{-7}$, which is below the range of accessible capillary numbers. Provided the contact angle is not too close to 90° , it is typically of this order for any dip-coating experiment since $\lambda \sim 10 - 20$ nm and $\ell_\gamma \sim 1 - 2$ mm. Therefore, dip-coating experiments run in the dynamic regime where k_ζ given by eqn (32) is appropriate. However, if instead of a plate we consider a thin fiber of radius $R \ll \ell_\gamma$ dipping into the bath, then the meniscus spring constant in the quasi-static limit is approximated by

$$k_\zeta \sim \frac{1}{R \ln(4\ell_\gamma/R)}. \quad (34)$$

In the case of a meniscus around a nano-fiber²², this is about four orders of magnitude higher than would be on a plate, i.e. eqn (28). The estimation for the dynamic spring constant in eqn (32) is independent of the external profile of the meniscus and we can find a cross-over capillary number for the fiber case as above:

$$\text{Ca}_{\text{co}} \sim \frac{\tan \theta_\mu}{6\pi \ln(4\ell_\gamma/R)} \frac{\lambda}{R}. \quad (35)$$

It is typically $\sim 10^{-2}$ and therefore in the upper-range of accessible capillary numbers. Thus, for such fiber experiments the static expression for the meniscus spring constant is appropriate.

2.7 Dissipative forces

Here we seek to physically motivate approximate expressions for the two dimensionless dissipative constants d_ζ and d_ψ . We refer the reader to²⁵ for full derivations. Here the dissipative forces per unit length associated with a displacement x take the form $-\eta d_x \dot{x}$. In general, they can be computed in the lubrication approximation by integrating the viscous stress over the disturbed interface. We expect that the dissipative constant then takes the

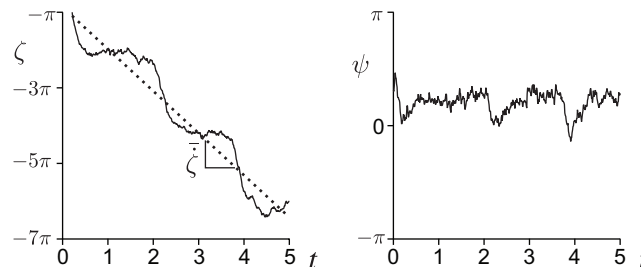


Fig. 4 Example time sequence for the two degrees of freedom ζ and ψ . Here the potential is taken as $qd = 0.7$ and $\mathcal{C} = 0.3$, with the dynamic parameters $\mathcal{T} = 2 \times 10^{-2}$, $D = 1$ and $F = -5$. (a) The dotted line indicates the time-averaged drift velocity.

form:

$$d \sim \frac{3 \ln \Lambda}{\tan \theta_\mu}, \quad (36)$$

where Λ is the ratio of the outer and inner scales over which the dissipation acts. The latter is generally expressed by a slip length ℓ_s .

First we consider the motion of the contact line when it is trapped in the potential well and attempting to hop the barrier via thermal fluctuations. The timescale associated with this fluctuating motion is given by the diffusion time over the spacing λ and leads to a much larger characteristic frequency $\omega \sim 2k_B T q^3 / \eta$ than previously used for the average global motion in section 2.6. Taking this as the dominant frequency for the dissipation process, the outer scale, as determined by the perturbation length, is therefore $\ell_U \sim \gamma / \eta \omega \sim \gamma / 2k_B T q^3$ and we take d_ζ given by:

$$d_\zeta \sim 3 \frac{\ln \left(1 + \frac{\gamma \lambda^3 \tan \theta_\mu \sin^3 \theta_\mu}{6k_B T (2\pi)^3 \ell_s \exp(4\gamma_{Euler} - 1/2)} \right)}{\tan \theta_\mu}, \quad (37)$$

where $\gamma_{Euler} \simeq 0.577$ is the Euler constant. One recognizes the form of eqn (36), with the logarithmic factor Λ involving an outer length proportional to $\gamma \lambda^3 / k_B T$ and an inner length set by the slip length ℓ_s .

Next we consider the deformation of the liquid-vapor interface to evaluate the dissipative constant associated with ψ . The dimensionless parameter d_ψ giving the viscous force applied to the free-surface distortion reads:

$$d_\psi \sim \frac{3}{\tan \theta_\mu} \frac{\ln \left(1 + \frac{\lambda \cos \theta_\mu \tan \theta_0}{6\pi \ell_s} \right)}{4 \ln^2(\lambda / 2\pi d)}, \quad (38)$$

The logarithmic factor in the numerator corresponds to Λ of eqn (36). Here it involves the wavelength λ as the outer length and ℓ_s as the inner length. The logarithmic term in the denominator results from the shape of the contact line and originates from the same term in the spring constant κ of eqn (25). Again, the additional dependencies can be obtained with a full derivation²⁵.

2.8 Dimensionless equations

In the previous sections we developed a two-dimensional model of thermally activated motion according to reaction path theory.

We provided approximate expressions for the coefficients controlling the restoring force in the case of an energy landscape reduced to periodic, Gaussian defects and showed that the Langevin equations take the generic form (1).

In anticipation of a parametric study, we make the Langevin equations (1) dimensionless. We use $d_\zeta \eta$, $k_B T$ and λ as units and render the equations dimensionless using $\lambda/2\pi = q^{-1}$ as a unit length, $\pi d_\zeta \eta / (k_B T q^3)$ as a unit time and therefore $k_B T q^2 / (\pi d_\zeta \eta)$ as a unit velocity. In order to avoid introducing new notations, we keep ζ and ψ for the rescaled quantities ($\zeta \rightarrow \zeta/q$, $\psi \rightarrow \psi/q$, $U \rightarrow U\pi d_\zeta \eta / (k_B T q^2)$ and $t \rightarrow t\pi d_\zeta \eta / (k_B T q^3)$):

$$D\dot{\psi} = \frac{1}{\mathcal{T}} \left[\mathcal{C} \exp \left[-\frac{(\zeta + \psi)^2}{2(qd)^2} \right] - \kappa\psi \right] + \sqrt{D}\mathcal{W}_\psi \quad (39)$$

$$\dot{\zeta} = \frac{F + \cos \theta_S}{\mathcal{T}} + \frac{\mathcal{C}}{\mathcal{T}} \exp \left[-\frac{(\zeta + \psi)^2}{2(qd)^2} \right] + \mathcal{W}_\zeta, \quad (40)$$

where $D = d_\psi/d_\zeta$ the ratio of the two dissipative constants and where the rescaled thermal energy \mathcal{T} reads:

$$\mathcal{T} = \frac{k_B T q^2}{\pi \gamma}. \quad (41)$$

For the experiment shown in Fig. 1 it is $\mathcal{T} \simeq 6.8 \times 10^{-3}$, which is small compared to $\mathcal{C} \simeq 0.1$ and therefore validates the thermal activation hypothesis, where the contact line gets trapped in the well before jumping the barriers.

Figure 4 shows an example time sequence of the dynamics of both ζ and ψ obtained numerically. For the chosen parameters, the contact-line dynamics are in the thermally activated regime, which can be recognized from the jumps and wait times seen in $\zeta(t)$. In fact, the contact line spends the majority of time stuck in a potential well, around a local equilibrium. The time-averaged drift velocity $\dot{\zeta}$ nevertheless corresponds to the imposed constant velocity of the plate U .

3 Reduction to a single degree of freedom

3.1 Langevin equation for a single degree of freedom

In the previous section, we have justified the form chosen for the Langevin equations (1) with two degrees of freedom. We now proceed with a further reduction of the parameter space, from two to only one degree of freedom, and then test the degree of validity of this reduction. The average position of the contact line ζ is the natural choice of reaction coordinate. To proceed, we assume that the distortions of the contact line are at equilibrium and therefore obtain the equations:

$$0 = \mathcal{C} \exp \left[-\frac{(\zeta + \psi)^2}{2(qd)^2} \right] - \kappa\psi \quad (42)$$

$$\dot{\zeta} = \frac{F + \cos \theta_S}{\mathcal{T}} + \frac{\mathcal{C}}{\mathcal{T}} \exp \left(-\frac{(\zeta + \psi)^2}{2(qd)^2} \right) + \mathcal{W}_\zeta \quad (43)$$

Equation (42), which was first introduced in the pioneering paper of Joanny and de Gennes²³, is an implicit equation relating the amplitude of the deformation ψ to the position ζ of the contact line. The solution to this equilibrium equation is represented

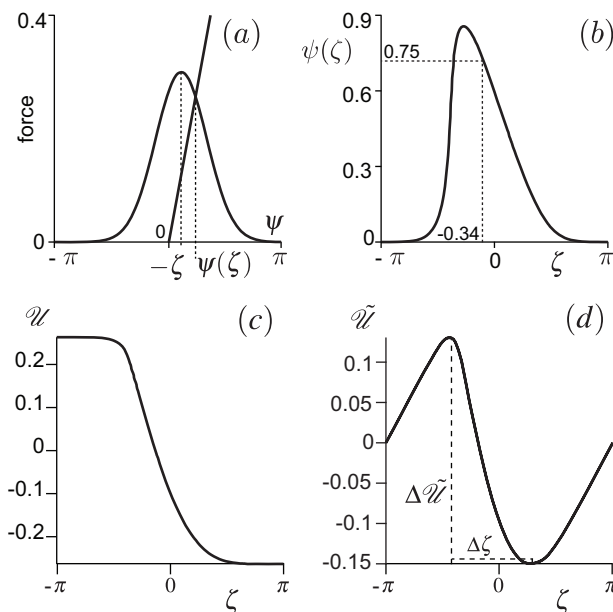


Fig. 5 (a) Graphical solution of the force balance eqn (42) between the distortion of the contact line and the defect strength for a defect characterized by $qd = 0.7$ and $\mathcal{C} = 0.3$ and for $\zeta = -0.34$. The solution $\psi(\zeta) = 0.75$ is the intersection point between the Gaussian and the line. (b) Here the defect is weak and for each position of the contact line there is a unique solution for the amplitude of the deformation. (c) The resulting potential. (d) In the calculation, the potential is then periodized such that the external work is due to the external force ΔF . $\Delta \tilde{\mathcal{U}}$ is defined as the height of the energy barrier and $\Delta \zeta$ the distance from the bottom of the well to the top of the barrier.

graphically in Fig. 5a. The dashed line corresponds to the elastic restoring force $\kappa\psi$ associated with the deformation of the liquid interface, which must match the force resulting from the presence of the solid, which here has been chosen to be Gaussian.

Defects are said to be *strong* if for at least one ζ , the equation admits several solutions ψ . Strong defects induce a multistable energy landscape while weak defects lead to a monostable energy landscape. Multistability occurs when the maximum slope of the Gaussian is larger than κ . The maximum slopes are located at $\psi = -\zeta + qd$ and $\psi = -\zeta - qd$ and their absolute value is $\frac{\mathcal{C}}{qd\sqrt{e}}$. The condition for defects to be weak is therefore

$$\mathcal{C} < qd\kappa\sqrt{e}. \quad (44)$$

The defect in the figure is *weak* since for any ζ there is a unique solution $\psi(\zeta)$, shown in Fig. 5b. The resulting potential is shown in Fig. 5c.

In the case of a strong defect, even in the absence of thermal activation, it is clear that the sequence of configurations taken by the contact line as it advances over a defect is not the same as when it recedes over that same defect. In other words, there is a hysteresis in the detailed position of the line since the deformation ψ at a given ζ depends on whether the contact line was moving in one direction or the other. The hysteresis in position is reflected in a difference in contact angle between advancing and receding directions. However, this separation between the two

branches of the dynamics is not unique to strong defects. Here we restrict ourselves to the case of a weak defect where there is no such hysteresis in position, the deformation is properly defined for each mean position of the contact line ($\psi(\zeta)$ is monovalued) and the reduced potential is $\mathcal{U}(\zeta) = \mathcal{U}(\zeta, \psi(\zeta))$. However, the defects still present energy barriers to motion and a minimum force (the zero-temperature depinning point) is necessary for the contact line to move in either direction. In addition, thermal-activation processes allow the line to overcome the defect before reaching the depinning point. As we shall see, this results in a separation between advancing and receding branches of the dynamics – such as shown at lower speeds for the weak defects in Fig. 1 – which is commonly referred to as contact angle hysteresis, but is in fact of different origin.

3.2 Mean-field force

In this section we seek to redefine the force by removing the mean-field contribution:

$$\Delta F = F + \cos \theta_0, \quad (45)$$

where θ_0 is the equilibrium angle, or what would be measured if the contact line were moving quasi-statically over the surface at constant instantaneous velocity ($\dot{\zeta} = U$). In this case, all of the contact line positions ζ are equally probable and the mean-field force can therefore be calculated by averaging eqn (23) over ζ :

$$\begin{aligned} \cos \theta_0 &\equiv \cos \theta_S + \int_{-\pi}^{\pi} \mathcal{C} \exp\left(-\frac{(\zeta + \psi(\zeta))^2}{2(qd)^2}\right) \frac{d\zeta}{2\pi} \\ &= \cos \theta_S + \frac{\mathcal{C}qd}{\sqrt{2\pi}} \operatorname{erf}\left[\frac{\pi}{\sqrt{2}qd}\right]. \end{aligned} \quad (46)$$

This redefinition has the advantage that ΔF then corresponds to the usual, experimental definition of the (dimensionless) unbalanced Young force: the difference in cosinus of angle between the equilibrium angle and the dynamic angle θ of the contact line. In practice, the positions ζ are not equally distributed as the contact line spends more time near the potential minimum. Following this redefinition, the potential must be modified so as to remove the contribution coming from the solid surface tensions that has been included in the new force variable. What remains is due to the force of the defect and the elastic restoring force, and it is therefore natural that it be periodic for our periodic effective landscape. The new potential is

$$\begin{aligned} \tilde{\mathcal{U}}(\zeta) &= \frac{1}{2} \kappa \psi(\zeta)^2 + \mathcal{C}qd \sqrt{\frac{\pi}{2}} \operatorname{erf}\left[-\frac{\zeta + \psi(\zeta)}{\sqrt{2}qd}\right] \\ &+ \zeta \frac{\mathcal{C}qd}{\sqrt{2\pi}} \operatorname{erf}\left[\frac{\pi}{\sqrt{2}qd}\right] \end{aligned} \quad (47)$$

and is illustrated in Fig. 5d. It is indeed periodic: the force due to defects does vanishing work when the contact line moves from one row of defects to another. The external work is only due to the external force ΔF . The Langevin equation then reads

$$\dot{\zeta} = \frac{\Delta F}{\mathcal{T}} - \frac{\tilde{\mathcal{U}}'(\zeta)}{\mathcal{T}} + \mathcal{W}_{\zeta}. \quad (48)$$

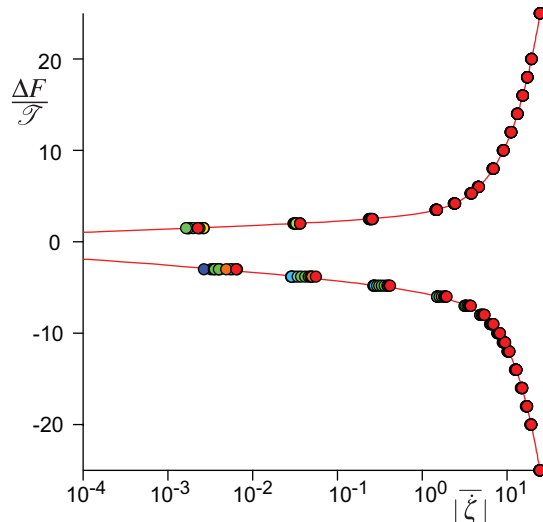


Fig. 6 Numerical solution of the Langevin equation with two degrees of freedom, for a fixed potential ($qd = 0.7$, $\mathcal{C} = 0.2$) and $\mathcal{T} = 2 \times 10^{-2}$ and for different values of the ratio D of dissipative constants: 10^{-3} to 10^3 from red to purple. The solid line is the exact solution of the Langevin equation reduced to a single reaction coordinate ζ given by eqn (49).

3.3 Constant force regime

For simplicity, we first examine the case of constant F , a choice that turns out to be the typical case in experiments for reasons that will be justified in the next section. In this case, the elastic restoring force of the large-scale meniscus is that of a wedge of angle θ_μ , given by eqn (6): $F = -\cos \theta_\mu$ and the Langevin equation (48) and has an exact solution²⁶ giving the average drift velocity as a function of the external force ΔF :

$$\bar{\zeta} = \frac{\pi(1 - e^{-4\pi\Delta F/\mathcal{T}})}{I_V I_{-V} - (1 - e^{-4\pi\Delta F/\mathcal{T}}) \int_{-\pi}^{\pi} e^{-2V(\zeta)} I_V(\zeta) d\zeta}, \quad (49)$$

where $\bar{\cdot}$ stands for the time average and

$$I_V(\zeta) \equiv \int_{-\pi}^{\zeta} e^{2V(\zeta')} d\zeta', \quad I_V \equiv I_V(\pi). \quad (50)$$

The biased potential V , defined with ζ over the interval $[-\pi, \pi]$, is

$$V(\zeta) = \frac{-\Delta F \zeta + \tilde{\mathcal{U}}(\zeta)}{\mathcal{T}}. \quad (51)$$

3.4 Comparison of the dynamics with one and two degrees of freedom

So far, the reaction path approach is an uncontrolled approximation for the dynamic contact line problem: are we really allowed to consider that most degrees of freedom relax faster than ζ ? We have the opportunity to investigate the quality of this approximation by comparing the results obtained while keeping the description based on two degrees of freedom (ζ and ψ) to those obtained with only a single one (ζ). We limit ourselves to weak defects associated with a monostable energy landscape when reduced to one degree of freedom. Figure 6 compares the relation

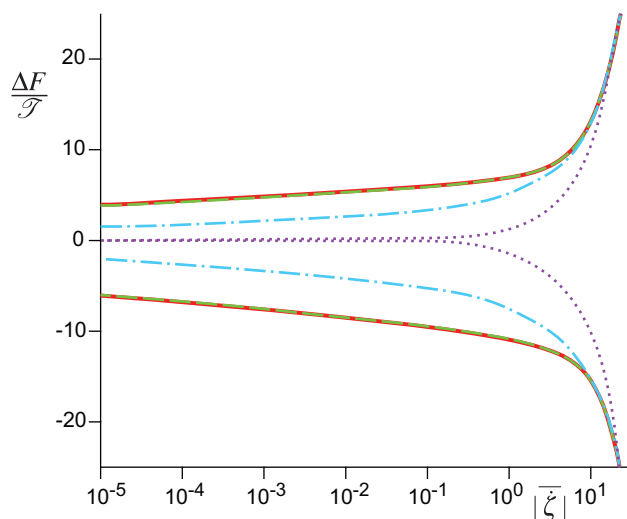


Fig. 7 Solutions the Langevin equation (43) for a fixed potential ($qd = 0.9$, $\mathcal{C} = 0.15$) and fixed temperature ($\mathcal{T} = 7.5 \times 10^{-3}$). The solid red line is the exact solution to the force driven Langevin equation given by eqn (49). The dotted and dashed lines are the solutions of the Langevin equation driven in velocity for different values of the spring constant. From the stiff spring to the soft spring; dotted purple line: $k_\zeta/q\mathcal{T} = 148$, dot-dashed blue line $k_\zeta/q\mathcal{T} = 2.7$, dashed green line $k_\zeta/q\mathcal{T} = 0.13$. For lower values of the spring constant, the force and velocity driven Langevin equations are equivalent.

between force and velocity obtained from (i) the numerical integration of the Langevin equation with two degrees of freedom and from (ii) the exact analytical formula of eqn (49) when the description is reduced to one degree of freedom. The timescale associated with the relaxation of the deformation ψ is controlled by the dimensionless number D . At vanishing D , one obtains perfect agreement between the two descriptions, as expected. Surprisingly, the agreement is still very good when ψ is the slowest variable, for $D > 1$. We have systematically tested the reduction as a function of \mathcal{C} and qd in the weak defect regime and conclude that the dynamics reduced to a single degree of freedom is an excellent approximation of the two-variable model. In the rest of the paper, we therefore restrain the discussion to the Langevin equation reduced to the reaction coordinate ζ .

3.5 Constant force versus constant velocity

We now investigate the difference between the equations solved at constant force F , given by eqn (6), and those at constant velocity U , where the force is given by eqn (27). Figure 7 shows the relation between the force and the average drift velocity obtained for constant force and for constant velocity with different values of the spring constant k_ζ . In the limit where the effective spring is soft ($k_\zeta/q\mathcal{T} \ll 1$), to reach the time-averaged velocity U and to overcome the force of the defects, the length of the effective spring, $(\bar{Z} + Ut - \zeta)$, must be large. As a consequence, its relative variations during the dynamics are small and the spring is essentially at constant elongation. Looking back at eqn (27) and Fig. 7, one observes that constant force and constant velocity are indeed equivalent in this limit. By contrast, in the limit where

the spring is rigid ($k_\zeta/q\mathcal{T} \gg 1$), by imposing the average velocity to be U , one also imposes the instantaneous velocity $\dot{\zeta} \simeq U$ (the length of the spring is small with large relative variations during the dynamics). The distribution of positions is homogeneous and the time averages during the dynamics becomes simple integrals over the period. The time average of eqn (43) gives:

$$\bar{\zeta} \simeq \frac{\Delta F}{\mathcal{T}}, \quad (52)$$

which is exactly the behavior observed for the purple dotted line ($k_\zeta/q\mathcal{T} = 148$) in Fig. 7: the dynamics doesn't exhibit a logarithmic-like behaviour but instead tends to a linear relation between the force and the velocity. In this case, thermal fluctuations have a negligible effect.

We now return to a typical experimental situation in order to determine if the criterion for a force-driven regime is easily realized. The dimensionless parameter that indicates the stiffness of the meniscus spring in a dip-coating experiment is

$$\frac{k_\zeta}{q\mathcal{T}} \sim \frac{3\eta\lambda^2 U}{4\pi \tan \theta_\mu k_B T} = \frac{3\gamma\lambda^2}{4\pi \tan \theta_\mu k_B T} \text{Ca}. \quad (53)$$

In the velocity-driven experiment shown in Fig. 1, the factor $\frac{3\gamma\lambda^2}{4\pi \tan \theta_\mu k_B T} \simeq 3 \times 10^2$. The ratio $k_\zeta/q\mathcal{T}$ consequently ranges from 3×10^{-5} to 3 in the experiment shown in Fig. 2. In other words, the crossover from a force-driven regime at small Ca to a velocity-driven regime at large Ca is around $\text{Ca} \simeq 10^{-3}$. This means that the majority of the experiment corresponds to a force-driven regime, with only the upper decade in Ca starting to feel the effect of a finite spring constant. In this case, even if the potential contains wells and barriers, the contact line can overcome these barriers via the meniscus spring that drives the contact line velocities, and not only by thermal activation.

The determination of whether an experiment is force or velocity driven also depends on the geometry of the system. In the case of a thin fiber, as discussed in section 2.6, it is more appropriate to use the static k_ζ and one consequently finds $k_\zeta/q\mathcal{T} \simeq 1$, i.e. in the rigid limit. It is therefore likely that dip-coating experiments on nano-fibers^{22,27} are driven in position and not in force.

4 Parametric study

We have shown that for weak defects, the thermally activated dynamics is well represented by a single reaction coordinate and by a dynamics at constant driving force. We now investigate the influence of the three independent parameters of the problem: the defect strength \mathcal{C} , its size compared to the distance between defects qd and the ratio \mathcal{T} comparing thermal effect to capillary effects.

4.1 Properties of the potential

The impact of the defect properties (\mathcal{C} and qd) on the dynamics, is produced through their effect on the shape of the potential. In anticipation of a parametric study, we reduce the description of the potential to the height of the barriers $\Delta\mathcal{U}$ and a distance between the top of the barrier and the bottom of the well $\Delta\zeta$ (see Fig. 5d). In this section we develop estimations of these two

quantities as a function of the defect properties. We will need the slope and curvature of the periodized potential:

$$\tilde{\mathcal{W}}'(\zeta) = -\kappa\psi(\zeta) + \frac{\mathcal{C}qd}{\sqrt{2\pi}}\operatorname{erf}\left[\frac{\pi}{\sqrt{2}qd}\right], \quad (54)$$

$$\tilde{\mathcal{W}}''(\zeta) = \frac{\kappa\psi(\zeta)(\zeta + \psi(\zeta))}{(qd)^2 + \psi(\zeta)(\zeta + \psi(\zeta))}, \quad (55)$$

where $\psi(\zeta)$ is obtained from eqn (42). The static equilibrium condition at zero temperature, $\tilde{\mathcal{W}}'(\zeta) = \Delta F$, admits solutions if the force is inside the range of the pinning forces:

$$\mathcal{C}\left(\frac{qd}{\sqrt{2\pi}}\operatorname{erf}\left[\frac{\pi}{\sqrt{2}qd}\right] - 1\right) < \Delta F < \mathcal{C}\frac{qd}{\sqrt{2\pi}}\operatorname{erf}\left[\frac{\pi}{\sqrt{2}qd}\right]. \quad (56)$$

This can be rewritten to explicitly introduce the depinning angles :

$$-\cos\Theta_a + \cos\theta_0 < \Delta F < -\cos\Theta_r + \cos\theta_0. \quad (57)$$

In this case, the total external potential contains minima (−) and maxima (+) whose locations are:

$$\zeta_{\pm} = -\psi(\zeta_{\pm}) \mp \sqrt{2}qd\sqrt{\ln\left[\frac{\mathcal{C}}{\kappa\psi(\zeta_{\pm})}\right]} \quad (58)$$

with

$$\psi(\zeta_+) = \psi(\zeta_-) = -\frac{\Delta F}{\kappa} + \frac{\mathcal{C}qd}{\kappa\sqrt{2\pi}}\operatorname{erf}\left[\frac{\pi}{\sqrt{2}qd}\right]. \quad (59)$$

For low forces, the distance $\Delta\zeta$ depends only on the rescaled defect size:

$$\Delta\zeta = \zeta_- - \zeta_+ \sim 2\sqrt{2}qd\sqrt{\ln\left[\frac{\sqrt{2\pi}}{qd\operatorname{erf}\left[\frac{\pi}{\sqrt{2}qd}\right]}\right]}. \quad (60)$$

From the locations of the extrema, one can easily find the barrier height. For low forces, we find that it is proportional to the defect amplitude \mathcal{C} and depends on qd through an increasing function that we denote α :

$$\Delta\tilde{\mathcal{W}} \sim \frac{\mathcal{C}\alpha(qd)}{2}, \quad (61)$$

which can be shown to be

$$\begin{aligned} \alpha(qd) \sim & 2\sqrt{2\pi}qd\operatorname{erf}\left(\sqrt{\ln\left(\frac{\sqrt{2\pi}}{qd\operatorname{erf}\left(\frac{\pi}{\sqrt{2}qd}\right)}\right)}\right) \\ & - \frac{4(qd)^2}{\sqrt{\pi}}\operatorname{erf}\left(\frac{\pi}{\sqrt{2}qd}\right)\sqrt{\ln\left(\frac{\sqrt{2\pi}}{qd\operatorname{erf}\left(\frac{\pi}{\sqrt{2}qd}\right)}\right)}. \end{aligned} \quad (62)$$

We will also need the product of curvatures at the extrema. For low forces, one can show that

$$|\tilde{\mathcal{W}}''(\zeta_+)\tilde{\mathcal{W}}''(\zeta_-)| \sim \frac{\mathcal{C}^2}{\pi}\operatorname{erf}\left[\frac{\pi}{\sqrt{2}qd}\right]^2\ln\left[\frac{\sqrt{2\pi}}{qd\operatorname{erf}\left[\frac{\pi}{\sqrt{2}qd}\right]}\right]. \quad (63)$$

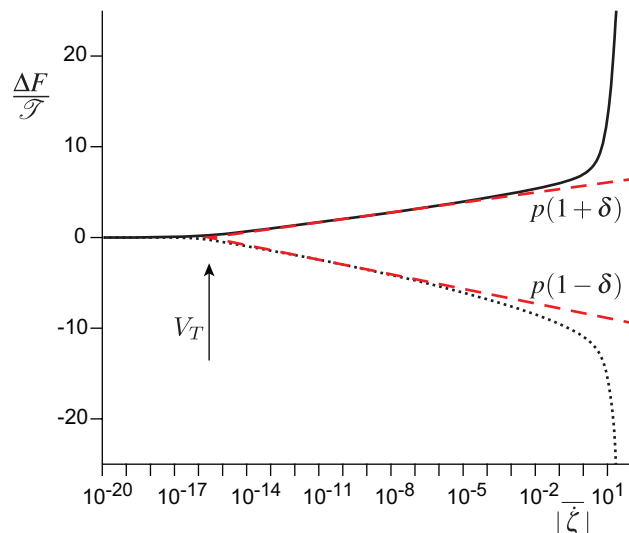


Fig. 8 Advancing (solid line) and receding (dotted line) dynamics according to the exact solution in eqn (49). The logarithmic portion of the branches, parametrised by eqn (64), are shown as dashed lines. p is defined as the mean slope of the log branches and δ their relative asymmetry. V_T is the thermal speed marking the transition between a linear response and the log regime. At higher driving force, the exact solution tends to a linear regime, where the potential and noise are negligible.

4.2 Force-velocity curve parametrization

Figure 8 shows a typical solution to the Langevin model found using the exact expression (49). It exhibits a regime with a logarithmic relation between force and velocity that is characteristic of a thermally activated process. Looking closely, one can see that the advancing and receding directions are asymmetric. For this reason, we choose to parametrize the advancing (+) and receding (−) log branches by

$$\bar{\zeta} = \pm V_T \exp\left[p(1 \pm \delta)\frac{|\Delta F|}{\mathcal{F}}\right], \quad (64)$$

in which three quantities are singled out: the mean slope of both branches p , the asymmetry of the slopes δ and the transition velocity where the two branches join V_T . Below V_T the system is close enough to thermal equilibrium for a linear response theory to be applicable. At higher driving force, the exact solution eqn (49) tends to a linear regime, where the potential and thermal noise are negligible. This high force regime is not described by the parametric log branches. We also note that it is unrelated to the onset of a regime dominated by hydrodynamic dissipation in the bulk meniscus¹⁵ since here we consider θ_μ and not the macroscopic angle directly measured in experiment.

4.3 Kramers' approximation for the transition velocity V_T

In this section, we perform a numerical study of the thermal transition speed V_T in order to determine its dependance on qd , \mathcal{C} and \mathcal{F} . The results are compared to the Kramers' rate theory, which gives the transition rate between wells of an arbitrary potential. Kramers' rate is based on an approximate description of the energy barriers using only the curvatures of the potential at

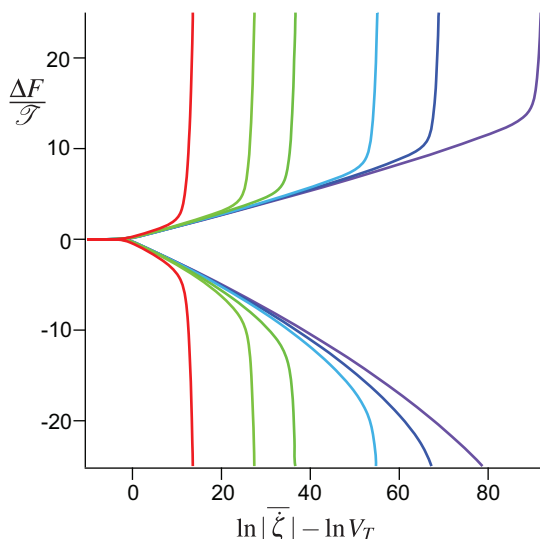


Fig. 9 Numerical exact solutions eqn (49) of the dynamics for a fixed potential ($qd = 0.7, \mathcal{C} = 0.3$) for different values of \mathcal{T} from low temperature (purple curve: $\mathcal{T} = 6.10^{-3}$) to moderate temperatures (red: $\mathcal{T} = 4.10^{-2}$). As the temperature decreases, the dynamics tend to Kramers' expression and the number of decades in the log regime diverges. For this potential, the speed has been rescaled according to $\ln V_T \simeq -0.55/\mathcal{T} + 3.5$ in order to collapse the curves.

the bottom of the well and at the top of the barrier, the height of the barrier $\Delta\tilde{\mathcal{U}}$ and the length $\Delta\zeta$. It assumes that the activated motion from one potential well to the other is a rare event i.e. that the thermal energy is small compared to the energy barrier. The advancing (+) and receding (−) dynamics are expressed as^{28 29}

$$\bar{\xi} \sim \pm \frac{\sqrt{|\tilde{\mathcal{U}}''(\zeta_+) \tilde{\mathcal{U}}''(\zeta_-)|}}{\mathcal{T}} \exp\left[\frac{-2\Delta\tilde{\mathcal{U}}}{\mathcal{T}}\right] \exp\left[2\Delta\zeta \frac{|\Delta F|}{\mathcal{T}}\right]. \quad (65)$$

The curvatures of the extrema determine the frequency at which the contact line tries to overcome the barrier while the height determines the probability of overcoming it. The length $\Delta\zeta$ controls the external work of the force ΔF when the contact line makes an elementary jump and therefore the bias induced in the potential by the external force. We first investigate the effect of the rescaled temperature \mathcal{T} , which impacts the dynamics by affecting the ratio between the amplitude of the potential and the thermal noise. Kramers' approximation of eqn (65) is an asymptotic solution valid at vanishing temperature and in which the number of decades where the dynamics exhibits a logarithmic behavior diverges. We compare this to the exact solution given by eqn (49) at different temperatures and for a fixed potential, i.e. given values of qd and \mathcal{C} . Fig. 9 shows that the number of decades where the dynamics exhibits a logarithmic behavior increases when the temperature decreases. Kramers' prediction for the transition speed reads:

$$\ln V_T \sim -\frac{2\Delta\tilde{\mathcal{U}}}{\mathcal{T}}. \quad (66)$$

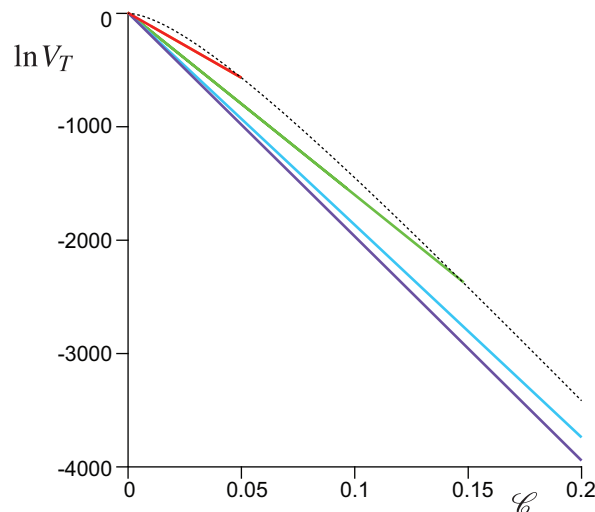


Fig. 10 Thermal transition speed $\ln V_T$ as a function of the defect strength \mathcal{C} at vanishing temperature ($\mathcal{T} = 10^{-4}$) for different values of the defect size qd (from purple to orange : $qd = 0.9, 0.7, 0.5, 0.3$). The curves are limited to the weak defect regime, the boundary of which is given by the dotted line.

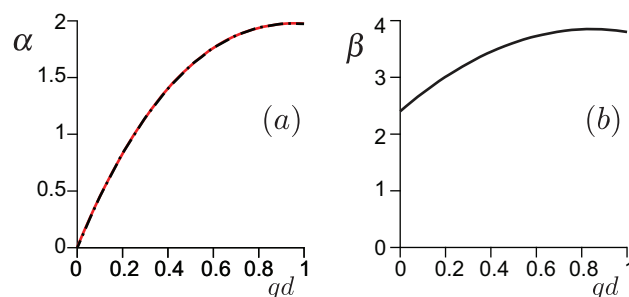


Fig. 11 Coefficients α and β defined in eqn (67). The dashed line is Kramers' prediction and the solid lines are obtained from (a) the slope and (b) the origin of curves such as those shown in Fig. 10.

In Fig. 9 – which is at fixed $\Delta\tilde{\mathcal{U}}$ – all of the curves obtained at low temperatures collapse at the transition when the velocity is rescaled by this. For higher temperatures, Kramers' approximation is not valid and the exact relation between force and velocity deviates from the asymptotic expression.

We now investigate the effect of the defect properties in the limit of vanishing temperature, where an asymptotic logarithmic behavior emerges. According to eqn (61), Kramers' approximation predicts that $\ln V_T$ depends linearly on the defect amplitude \mathcal{C} . Fig. 10 shows that the numerical results confirm this. The dependence of the slope and the value at origin can be studied as a function of the second parameter, qd . Formally we write

$$\ln V_T \simeq -\alpha(qd) \frac{\mathcal{C}}{\mathcal{T}} + \beta(qd). \quad (67)$$

Figure 11a shows that the function $\alpha(qd)$ is perfectly predicted by Kramers'. Subdominant dependencies are embedded in the constant β , which principally depends on qd .

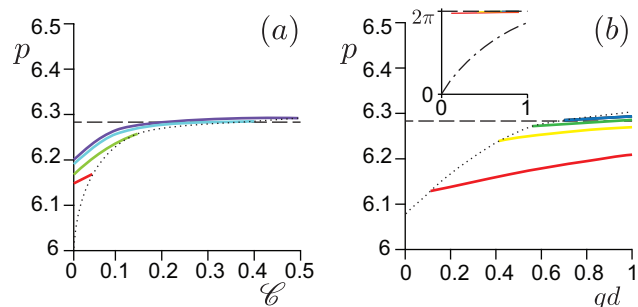


Fig. 12 Mean slopes of the logarithmic regimes of the dynamics in the low-temperature limit (here $\mathcal{T} = 10^{-4}$). (a) As a function of the defect amplitude \mathcal{E} for a series of defect sizes qd (from purple to red: $qd = 0.9, 0.7, 0.5, 0.3$). (b) As a function of qd for a series of \mathcal{E} (from purple to red: $\mathcal{E} = 0.01, 0.1, 0.2, 0.4$). The dotted lines delimit the boundary between weak and strong defects. The dashed horizontal lines are the exact results for a ratchet potential using eqn (49). The dashed-dotted line in the inset shows Kramers' prediction of eqn (68).

4.4 Logarithmic slopes of the force-velocity relation

The slopes of the logarithmic branches introduced in eqn (64) are well defined in the limit of vanishing temperature. For low enough temperatures, Fig. 9 shows that the slopes are invariant with the temperature. We investigate the dependence of these logarithmic slopes on the defect properties in the asymptotic limit of vanishing temperature – in practice, figures are plotted for $\mathcal{T} = 10^{-4}$. First we compare to Kramers' prediction, then we show that a better model is the exact formula on a ratchet potential.

Figure 12 shows that the average slope p depends only weakly on qd and \mathcal{E} : over the full possible scale of these parameters, the variation is at most 3% from $p \simeq 2\pi$. It does not behave according to Kramers, which predicts

$$p = 2\Delta\zeta \sim 4\sqrt{2}qd \sqrt{\ln \left[\frac{\sqrt{2\pi}}{qd \operatorname{erf} \left[\frac{\pi}{\sqrt{2}qd} \right]} \right]}, \quad (68)$$

giving a mean slope nearly proportional to qd . The orders of magnitude are inconsistent as well as one can see in the insert of Fig. 12b, where the dotted-dashed line represents the Kramers' prediction.

Figure 13 shows that the asymmetry between advancing and receding directions results only from the rescaled defect size qd and does not depend on the scale-free amplitude of the defect \mathcal{E} . Again, this is not consistent with Kramers' approximation which, being based on a Taylor expansion of the potential to quadratic order, predicts perfectly symmetric curves in the advancing and receding directions. Examining the invariances and symmetries of the exact solution given by eqn (49), one can see that the advancing and receding dynamics are asymmetric if the potential does not contain an axis of vertical symmetry, i.e., if the shapes of the maxima and minima contains odd terms in their development. To improve the modeling, we have therefore studied the force-velocity relation for the simplest potential that contains such an asymmetry: the ratchet or *saw-tooth* potential. Just like the Kramers potential, it can be described by an amplitude $\Delta\mathcal{U}$

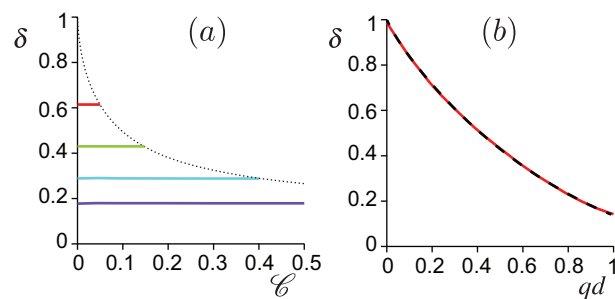


Fig. 13 Asymmetry of the slopes δ between the advancing and receding branches in the log regime in the low-temperature limit (here $\mathcal{T} = 10^{-4}$). (a) As a function of the defect height \mathcal{E} for a series of defect sizes qd (from purple to red: $qd = 0.9, 0.7, 0.5, 0.3$). The dotted line delimits the boundary between weak and strong defects. (b) As a function of qd . The dashed line is the exact prediction of eqn (49) for a ratchet potential.

and a distance between the well and barrier $\Delta\zeta$ and one can analytically determine the force-velocity relationship in eqn (49). In the limit of vanishing temperature one obtains

$$\bar{\xi} \sim \pm \frac{\Delta\mathcal{U}^2}{\pi\mathcal{T}^2} \exp \left[\frac{-2\Delta\mathcal{U}}{\mathcal{T}} \right] \exp \left[(2\pi \pm (2\pi - 2\Delta\zeta)) \frac{|\Delta F|}{\mathcal{T}} \right]. \quad (69)$$

The height $\Delta\mathcal{U}$ still controls the probability of overcoming the energy barrier, and therefore the prediction for the transition velocity V_T in eqn (66) is unchanged. However, in this case, the log branches have a constant mean slope, independent of the barrier height and length:

$$p = 2\pi, \quad (70)$$

and an asymmetry that depends only on the distance between the barrier and well:

$$\delta = 1 - \frac{\Delta\zeta}{\pi}, \quad (71)$$

where $\Delta\zeta$ is still given by eqn (60). Figure 13 shows that this constitutes an excellent approximation of the curves obtained with the actual potential, although the actual potential only looks like a ratchet for small values of qd .

5 Returning to experiments

5.1 Scaling relations in the thermal asymptotic regime

After having worked with rescaled quantities above, in this section we provide the expression for the logarithmic regime using the original input parameters. Experiments measuring contact line dynamics can be reported in terms of the contact angle $\cos \theta_\mu$ as a function of the capillary number Ca . In the asymptotic limit of thermal activation (i.e. at vanishing temperature), we have shown that the relation takes the form

$$Ca = \pm Ca_T \exp \left[(1 \pm \delta) \frac{\gamma\lambda^2 |\cos \theta_0 - \cos \theta_\mu|}{2k_B T} \right]. \quad (72)$$

One recognizes the general Arrhenius form that has been frequently used to fit experimental data. The significant advancement here is that we have rationalized the full expression and we give explicit expressions for the transition Ca_T and for the asymmetry δ between the advancing and receding branches,

which is not ad-hoc but appears as a natural consequence of the model. One can also recognize that the distance between defects λ controls the mean slope of both branches taken together.

Specifically, we have shown that the asymmetry is controlled by the size of the defect d relative to λ :

$$\delta \simeq 1 - 4 \frac{d}{\lambda} \sqrt{2 \ln \left[\frac{\lambda}{d \sqrt{2\pi} \operatorname{erf} \left[\frac{\lambda}{d 2\sqrt{2}} \right]} \right]}. \quad (73)$$

It is notably insensitive to the scale-free strength of the defects and in particular to whether they are very weak or near the limit of being strong. The larger d/λ the more symmetrical the two branches are.

The prefactor in eqn (72) is a transition capillary number corresponding to the point where the two branches join. It scales as

$$\text{Ca}_T = \frac{4\pi}{d_\zeta} \frac{k_B T}{\gamma \lambda^2} \exp \left[-\frac{\alpha \mathcal{C}}{2\pi} \frac{\gamma \lambda^2}{2k_B T} + \beta \right], \quad (74)$$

where the coefficient α depends on the rescaled size of the defect $qd = 2\pi d/\lambda$ according to eqn (62) and β varies only weakly with qd .

The scale-free defect strength \mathcal{C} linearly controls the intersection point of the advancing and receding branches in $\ln \text{Ca}_T$, or equivalently the separation (i.e. difference in force $\cos \theta_\mu$) between the branches at the same speed. From eqn (56) we see that \mathcal{C} also controls the depinning angles:

$$\cos \Theta_a - \cos \Theta_r = \mathcal{C}. \quad (75)$$

Finally, it selects the capillary number $\text{Ca} \sim \mathcal{C}/d_\zeta$ at which the cross-over from the activated regime to the high velocity linear regime takes place.

The friction coefficient d_ζ appearing in Ca_T is given by eqn (37) and is smaller than unity ($d_\zeta \simeq 0.7$). Physically, it corresponds to the viscous friction associated with the global motion (ζ) of the contact line. We note that this is an evolution with respect to our previous, preliminary report of this model¹⁵ in which we proposed a Langevin description based upon a single variable (ζ) but erroneously attributed the extra viscous dissipation as arising from the fluctuations of the interface (ψ). The four fit parameters ($\cos \theta_0$, λ , δ , Ca_T) appearing in eqn (72) can therefore be used to uniquely determine the four physical parameters of the model ($\cos \theta_0$, λ , d , \mathcal{C}) given d_ζ , α and β .

5.2 Adjusting experimental data

Once an experiment has been performed and the dynamics plotted, one can ask what dynamical regimes were accessed, and in particular, over what range of Ca can the asymptotic expression of eqn (72) be used to fit the data. Most often, experiments are reported in terms of the macroscopic angle and show what looks like two regimes with a crossover (a batwing). However, it is not immediately clear if this is indeed a crossover between a thermally activated regime and a hydrodynamic one, or if the experiment explores the thermally activated regime beyond the depinning threshold. Without any knowledge *a priori* of λ , d , \mathcal{C}

and $\cos \theta_0$, one must fit to find out. First one must deduce θ_μ by subtracting the viscous force resulting from all scales between the molecular scale and the capillary length, a procedure that has been outlined elsewhere¹⁵. For sufficiently low Ca we note that the macroscopic and effective microscopic angles are confounded. If the batwing remains in the dynamics of θ_μ , then the experiment approaches the depinning threshold. If not, care must still be taken to first check that the range of Ca is low enough that a purely logarithmic regime applies before using eqn (72).

The solid lines in Fig. 1 correspond to a numerically calculated fit of both branches to the full model represented by eqn (49). The dashed lines in the same figure correspond to the asymptotic limit of thermal activation for the same fit parameters. From the non-overlap of the solid and dashed lines, one can see that the experimental data – the receding branch in particular – lie outside of the purely exponential limit. If we were to have fit to the asymptotic form of eqn (72), the fit parameters would not correspond to the real physical parameters. Since the disparity between the full solution and the asymptotic form over the range of experimental Ca is relatively small it is possible to make use of the asymptotic form developed here to properly extract the real parameters of the energy landscape and avoid the necessity of implementing a numerical fitting procedure to eqn (49). To do so, one can use an iterative procedure to find how each parameter of the full model maps to the fit parameters when the full model is fit to the form eqn (72) over the experimental range of Ca .^{*} The uncertainties in the model parameters can be evaluated either directly from the statistical errors in the fit to eqn (72) (λ , $\cos \theta_0$) or from their propagation through eqns (73) and (74) (d and \mathcal{C}). Considering only the statistical errors and using this method to propagate them, the best fit parameters to the data in Fig. 1 are $\lambda = 18 \pm 0.5$ nm, $\cos \theta_0 = 0.569 \pm 0.002$, $d = 2.0 \pm 0.3$ nm and $\mathcal{C} = 0.122 \pm 0.002$. These parameters observe the condition in eqn (44) so the defects are indeed weak.

6 Conclusion

Beginning from a two-variable Langevin description of the dynamic contact line problem, we have developed a working model to fit thermally activated motion in the purely logarithmic regime and beyond. We have worked with weak defects, for which we have shown that a one-variable description is an excellent approximation, and we have clarified the distinct concepts of hysteresis (which is not present for weak defects) and the experimental observation of the separation between the advancing and receding branches of the dynamics (which is).

In developing the model, we left open the possibility to either

^{*} The iterative procedure is as follows: one fits the data to the asymptotic form and injects the resulting parameters ($\cos \theta_0$, λ_0 , δ_0 , Ca_{T0}) into the full solution of eqn (49). The resulting full curve is then fit to the asymptotic form again to output new fit parameters ($\cos \theta_0$, λ_n , δ_n , Ca_{Tn}). The new asymptotic curve will be shifted and scaled with respect to the original one. One uses the shift to adjust $\cos \theta_0$ and $\ln \text{Ca}_T$ and the scaling to adjust λ and δ for the next input parameters to the full model (i.e. $\cos \theta_{0n+1} = \cos \theta_0 + \sum_1^n (\cos \theta_0 - \cos \theta_{0i})$ or $\lambda_{n+1} = \lambda_0 \prod_1^n \frac{\lambda_0}{\lambda_i}$ etc.). One iterates until convergence, at which point the full solution with physical parameters ($\cos \theta_n$, λ_n , d_n , \mathcal{C}_n) will yield the original experimental fit parameters ($\cos \theta_0$, λ_0 , δ_0 , Ca_{T0}) when fit by eqn (72).

force or velocity driving. By examining the meniscus stiffness, we later showed that dip-coating experiments in the plate geometry are in fact driven in force. For the case of weak defects in force driving, an exact solution to the model exists. We performed a parametric study of the asymptotic limit of this solution corresponding to vanishing temperature. We find a purely logarithmic regime that resembles the Arrhenius-type models commonly used in the field. The added value here is that we provide rationalized expressions for the prefactor, and for the asymmetry between advancing and receding branches that is so frequently observed in experiment. We also show that the depinning angles are determined by the scale-free strength of the defect. Important practical lessons that come from studying the model in this limit are that (1) one needs both the advancing and receding branches in order to determine λ since it is related to the *mean* slope and (2) for each experiment, one must verify that the conditions indeed correspond to the asymptotic regime. Using the exact solution to fit to our experimental data reaching as low as $\text{Ca} \simeq 10^{-7}$, we find that the purely logarithmic regime is at still lower Ca , and thus suspect this to be the case in many experiments. We propose a procedure to use a fit to the simpler asymptotic form even outside of its region of validity which, when used in combination with the exact solution, can correctly extract the physical parameters of the model.

The problem of a moving contact line is both multi-scaled and multi-frequency. For example, the dimensionless friction coefficient d_ζ depends on the frequency of oscillation of the contact line. In this article, when necessary, we have used physical arguments to justify the choice of a single length or frequency scale in order to render the problem tractable and obtain practical, working expressions that can be used to analyse experimental data. In the case of d_ζ , we argued that the contact line spends the majority of the time stuck in a potential well and therefore the thermal attempt frequency is dominant over, say, the success rate for overcoming the barrier. This is appropriate in the logarithmic limit that we focus on here, but clearly would not be appropriate in the high-force regime, beyond depinning. In this sense, we recognise that the full problem is in fact richer and more complicated than presented here. Another method used here to simplify the problem is the mapping of a real, random, multi-scale energy landscape to an effective landscape with periodic, Gaussian defects. It remains an outstanding question how to link the model fit parameters to measurable properties of the physical or chemical defects on a real solid surface.

Acknowledgments. The authors gratefully acknowledge Jacco Snoeijer for many discussions. B.A. is supported by Institut Universitaire de France. This work was funded by the ANR grants Smart and REALWET.

References

- 1 D. Bonn, J. Eggers, J. Indekeu, J. Meunier and E. Rolley, *Rev. Mod. Phys.*, 2009, **81**, 739.
- 2 P.-G. de Gennes, F. Brochard-Wyart and D. Quere, *Capillarity and wetting phenomena: drops, bubbles, pearls, waves*, Springer, New York, 2004.
- 3 J. H. Snoeijer and B. Andreotti, *Ann. Rev. Fluid Mech.*, 2013, **45**, 269–92.
- 4 T. D. Blake and J. M. Haynes, *J. Colloid Interface Sci.*, 1969, **30**, 421–423.
- 5 E. Rolley and C. Guthmann, *Phys. Rev. Lett.*, 2007, **98**, 166105.
- 6 A. Giacomello, L. Schimmele and S. Dietrich, *Proceedings of the National Academy of Sciences*, 2016, **113**, E262–E271.
- 7 T. D. Blake and J. De Coninck, *The European Physical Journal Special Topics*, 2011, **197**, 249.
- 8 K. Davitt, M. S. Pettersen and E. Rolley, *Langmuir*, 2013, **29**, 6884–6894.
- 9 M. Ramiasa, J. Ralston, R. Fetzner, R. Sedev, D. M. Fopp-Spori, C. Morhard, C. Pacholski and J. P. Spatz, *Journal of the American Chemical Society*, 2013, **135**, 7159–7171.
- 10 P. de Gennes, *Physica A: Statistical Mechanics and its Applications*, 1998, **249**, 196 – 205.
- 11 G. Kumar and K. N. Prabhu, *Advances in Colloid and Interface Science*, 2007, **133**, 61 – 89.
- 12 M. Shanahan, *Journal of Physics D Applied Physics*, 1988, **21**, 981.
- 13 E. Agoritsas, V. Lecomte and T. Giamarchi, *Physica B: Condensed Matter*, 2012, **407**, 1725 – 1733.
- 14 A. Rosso and W. Krauth, *Phys. Rev. E*, 2002, **65**, 025101(R).
- 15 H. Perrin, R. Lhermerout, K. Davitt, E. Rolley and B. Andreotti, *Phys. Rev. Lett.*, 2016, **116**, 184502.
- 16 M. Voué, R. Rioboo, M. H. Adao, J. Conti, A. I. Bondar, D. A. Ivanov, T. D. Blake and J. De Coninck, *Langmuir*, 2007, **23**, 4695–4699.
- 17 M. Ramiasa, J. Ralston, R. Fetzner and R. Sedev, *The Journal of Physical Chemistry C*, 2012, **116**, 10934–10943.
- 18 J. G. Petrov, J. Ralston, M. Schneemilch and R. A. Hayes, *The Journal of Physical Chemistry B*, 2003, **107**, 1634–1645.
- 19 M.-J. Vega, D. Seveno, G. Lemaire, M.-H. Adão and J. De Coninck, *Langmuir*, 2005, **21**, 9584–9590.
- 20 S. Ray, R. Sedev, C. Priest and J. Ralston, *Langmuir*, 2008, **24**, 13007–13012.
- 21 E. Raphaël and P. G. de Gennes, *The Journal of Chemical Physics*, 1989, **90**, 7577–7584.
- 22 J. Dupré de Baubigny, M. Benzaquen, L. Fabié, M. Delmas, J.-P. Aimé, M. Legros and T. Ondarçuhu, *Langmuir*, 2015, **31**, 9790–9798.
- 23 J.-F. Joanny and P.-G. de Gennes, *J. Chem. Phys.*, 1984, **81**, 552–562.
- 24 J. Crassous and E. Charlaix, *EPL (Europhysics Letters)*, 1994, **28**, 415.
- 25 H. Perrin, D. Belardinelli, M. Sbragaglia and B. Andreotti, *arXiv:1708.01757*, 2017.
- 26 H. Risken, *The Fokker-Planck Equation - Methods of Solution and Applications*, Springer, 1984.
- 27 M. Delmas, M. Monthieux and T. Ondarçuhu, *Phys. Rev. Lett.*, 2011, **106**, 136102.
- 28 H. A. Kramers, *Physica*, 1940, **7**, 284.
- 29 P. Hänggi, P. Talkner and M. Borkover, *Reviews of Modern Physics*, 1990, **62**, 251.